Nanoscale

PAPER

View Article Online
View Journal | View Issue

Cite this: *Nanoscale*, 2014, **6**, 9166

Observation of the origin of d^0 magnetism in ZnO nanostructures using X-ray-based microscopic and spectroscopic techniques†

Shashi B. Singh,‡§[a] Yu-Fu Wang,‡[a] Yu-Cheng Shao,[a] Hsuan-Yu Lai,[a] Shang-Hsien Hsieh,[a] Mukta V. Limaye,[a] Chen-Hao Chuang,[a] Hung-Chung Hsueh,*[a] Hsaiotsu Wang,[b] Jau-Wern Chiou,*[c] Hung-Ming Tsai,[d] Chih-Wen Pao,[d] Chia-Hao Chen,[d] Hong-Ji Lin,[d] Jyh-Fu Lee,[d] Chun-Te Wu,[e] Jih-Jen Wu,[e] Way-Faung Pong,*[a] Takuji Ohigashi,[f] Nobuhiro Kosugi,[f] Jian Wang,[g] Jigang Zhou,[g] Tom Regier[g] and Tsun-Kong Sham[h]

Efforts have been made to elucidate the origin of d^0 magnetism in ZnO nanocactuses (NCs) and nanowires (NWs) using X-ray-based microscopic and spectroscopic techniques. The photoluminescence and O K-edge and Zn $L_{3,2}$-edge X-ray-excited optical luminescence spectra showed that ZnO NCs contain more defects than NWs do and that in ZnO NCs, more defects are present at the O sites than at the Zn sites. Specifically, the results of O K-edge scanning transmission X-ray microscopy (STXM) and the corresponding X-ray-absorption near-edge structure (XANES) spectroscopy demonstrated that the impurity (non-stoichiometric) region in ZnO NCs contains a greater defect population than the thick region. The intensity of O K-edge STXM-XANES in the impurity region is more predominant in ZnO NCs than in NWs. The increase in the unoccupied (occupied) density of states at/above (at/below) the conduction-band minimum (valence-band maximum) or the Fermi level is related to the population of defects at the O sites, as revealed by comparing the ZnO NCs to the NWs. The results of O K-edge and Zn $L_{3,2}$-edge X-ray magnetic circular dichroism demonstrated that the origin of magnetization is attributable to the O 2p orbitals rather than the Zn d orbitals. Further, the local density approximation (LDA) + U verified that vacancies in the form of dangling or unpaired 2p states (due to Zn vacancies) induced a significant local spin moment in the nearest-neighboring O atoms to the defect center, which was determined from the uneven local spin density by analyzing the partial density of states of O 2p in ZnO.

Received 11th April 2014
Accepted 25th May 2014

DOI: 10.1039/c4nr01961j

www.rsc.org/nanoscale

Introduction

In the past, numerous efforts have been made to develop diluted magnetic semiconductors that can support spin transport at or above room temperature by means of the magnetic doping of semiconductor materials.[1–4] However, the role of possible extrinsic (magnetic atom segregation, *etc.*) and/or intrinsic room-temperature ferromagnetism in these materials is not yet fully understood.[1,5] New complexity has been introduced by the observation of ferromagnetism in undoped semiconductor thin films and nanostructures.[6] In recent years, the d^0 magnetism of nanomaterials has been considered to be one of the most interesting and challenging phenomena that may provide an avenue for investigating and understanding the origin of nanomagnetism.[7–9] Venkatesan *et al.*[6] have observed d^0 magnetism in HfO_2 thin films and have triggered extensive experimental activities in the field of the room-temperature ferromagnetism of many semiconductors and nanomaterials. Magnetism has been reported in various nonmagnetic oxides,[6,10] selenides[11,12] and Au-metal nanoparticles.[13,14] Among

[a]*Department of Physics, Tamkang University, Tamsui 251, Taiwan. E-mail: hchsueh@mail.tku.edu.tw; jwchiou@nuk.edu.tw; wfpong@mail.tku.edu.tw*
[b]*Department of Physics, National Tsinghua University, Hsinchu 300, Taiwan*
[c]*Department of Applied Physics, National University of Kaohsiung, Kaohsiung 811, Taiwan*
[d]*National Synchrotron Radiation Research Center, Hsinchu 300, Taiwan*
[e]*Department of Chemical Engineering, National Cheng Kung University, Tainan 701, Taiwan*
[f]*Institute for Molecular Science, Okazaki 444-8585, Japan*
[g]*Canadian Light Source Inc., Saskatchewan S7N 2V3, Canada*
[h]*Department of Chemistry, University of Western Ontario, London N6A 5B7, Canada*

† Electronic supplementary information (ESI) available: Scanning photoelectron microscopy (SPEM) results of ZnO NCs and NWs. Computational details and calculated total and partial density of states (PDOS) of bulk wurtzite ZnO with oxygen anion vacancies (V_O). See DOI: 10.1039/c4nr01961j

‡ These authors contributed equally to this work.

§ Presently at Department of Physics, Indian Institute of Science Education and Research, Bhopal, India.

them, magnetism in ZnO has also been studied more than that of any other compound or semiconductor.[7–9] Surface-capping molecules,[7,15] defects and/or vacancies[6,10] are considered to be very important causes for d^0 magnetism in ZnO nanostructures and thin films. The origin of magnetization in ZnO and the role of surface defects,[16] O vacancies (V_O),[6,17,18] Zn vacancies (V_{Zn}),[19,20] and so on in the d^0 magnetism mechanism remain the topics of controversy. Keavney *et al.*[21] have used the Cu, Zn $L_{3,2}$- and O K-edge X-ray magnetic circular dichroism (XMCD) techniques and found no XMCD signal in a Cu-doped ZnO thin film. They have also reported the absence of any magnetic moment at either the Zn or O sites and only a small paramagnetic contribution to the Cu 3d orbitals, which is prevalent at the surface of the ZnO film. Chaboy *et al.*[22] have verified the role of the conduction band in the magnetism and have ruled out the possibility of a valence band (basically, Zn 3d orbitals) in thiol-capped ZnO nanoparticles by performing a Zn K-edge XMCD measurement. They found that the occurrence of magnetism was related to the structural modification at the interface between the nanoparticles and the capped molecules. The intrinsic ferromagnetic behavior at room temperature has been observed in various complex (capped with organic molecules and core–shell-structured) ZnO nanostructures using the XMCD technique.[23] The variation of vacancies in ZnO films with varying N_2 pressure has also been observed *via* positron annihilation spectroscopy.[20] Nonetheless, the controversy related to anion and cation vacancies in d^0 magnetism also exists in the theoretical calculations.[24–29] Specifically, Wang *et al.*[24] have utilized density functional theory (DFT) calculations to demonstrate the role of V_{Zn}, which induces spin polarization at the top of the valence band in d^0 magnetism. Morozovska *et al.*[26] have suggested that both V_O and V_{Zn} are involved in the magnetism because of their triplet ground state and Hund's rule. On the other hand, Podila *et al.*[29] using the *ab initio* calculations highlighted the role of the sample preparation method and annealing conditions in the origin and tuning of magnetism in ZnO. The origin of d^0 magnetism in ZnO is still not clearly understood, and most of the available explanations of d^0 magnetism as induced by surface characteristics or defects are drawn based on bulk-sensitivity experimental techniques [such as photoluminescence (PL), magnetic-hysteresis (M–H) curve measurements, *etc.*]. A ZnO nanostructure is the ideal system to study and gain an understanding of the role of defects and/or vacancies present in the edge or surface regions in d^0 magnetism, as such a nanostructure has a large edge- or surface-to-volume ratio. However, spatially resolved and element-specific microscopic and spectroscopic techniques are required to discriminate electronic structures between surface and core effects in nanostructures and also able to identify defects and/or vacancies in a particular region and at the sites of a specific element, thus directly providing evidence related to d^0 magnetism in ZnO nanostructures.

In this work, ZnO nanocactuses (NCs) and nanowires (NWs) are extensively studied using X-ray-based microscopic and spectroscopic techniques to probe the defects and/or vacancies in specific regions and at specific sites in terms of their chemical states, electronic structures and magnetic moments, which are closely related to the origin of d^0 magnetism in ZnO nanostructures. The X-ray-based microscopic and spectroscopic techniques used in this study include extended X-ray-absorption fine structure (EXAFS) spectroscopy, X-ray-excited optical luminescence (XEOL) spectroscopy, scanning transmission X-ray microscopy (STXM) and the corresponding X-ray-absorption near-edge structure (XANES) spectroscopy. The main advantage of the use of STXM-XANES in this work is its ability to map chemical states and determine spatially resolved electronic structures in a selected area and site of interest, and these are typically extracted from image masks applied to the STXM data.[30,31] Scanning photoelectron microscopy (SPEM) and XMCD measurements were also performed, and they supported the claim that defects and/or vacancies and O 2p orbitals are playing critical roles in inducing d^0 ferromagnetism in ZnO nanostructures. These findings provide conclusive evidence that the strength of d^0 magnetism in ZnO nanostructures is determined not only by V_{Zn} in the surface/edge (non-stoichiometric) regions but also by the population of defects and/or vacancies. The local density approximation (LDA) + U calculations further confirm that dangling and/or unpaired O 2p states that arise because of V_{Zn}, rather the Zn 3d orbitals and V_O, are primarily responsible for d^0 magnetism in ZnO nanostructures.

Experimental

Sample preparation

Aligned ZnO NW arrays were grown on seeded fluorine-doped tin oxide (FTO) substrates *via* chemical bath deposition (CBD) in a 0.02 M aqueous solution of zinc acetate and hexamethylenetetramine at 95 °C for 3 h. A limpid solution, which was obtained by diluting a solution of 0.57 M $ZnAc \cdot 2H_2O$ and 5 M NaOH by a factor of 10, was prepared for the subsequent CBD. The ZnO NW array was immersed in the stirred limpid solution at room temperature (RT) for 20 min. The spines were directly formed on the ZnO NWs, and the diameters of the NWs were also slightly increased after RT CBD. A hierarchical ZnO array, referred to as a ZnO NC array, was then formed on an FTO substrate. In order to fabricate ZnO NCs, the second CBD experiment was performed on the top of ZnO NWs, during this process RT CBD is performed by using ZnAc and NaOH as precursors. The synthesis, morphology and characteristics of the ZnO NC and NW samples are described elsewhere.[32]

X-ray-based microscopic and spectroscopic experiments and sample characterization

Zn K-edge EXAFS spectra, SPEM and O K-edge and Zn $L_{3,2}$-edge XMCD were collected at the Wiggler-17C, Undulator-09A and Dragon-11A beamlines, respectively, at the National Synchrotron Radiation Research Center in Hsinchu, Taiwan. The Zn K-edge EXAFS spectra were obtained in fluorescence mode, while the O K-edge and Zn $L_{3,2}$-edge XMCD spectra were obtained in surface-sensitive electron-yield mode. The angle of incidence of the X-rays was fixed at 30° from the sample normal, and a magnetic field of 1 tesla was applied parallel and anti-parallel to the sample normal throughout the XMCD

measurements. The resolution was set to ~0.1 eV (0.2 eV) at a photon energy of 530 eV (1020 eV) for the O K-edge (Zn $L_{3,2}$-edge) XANES measurements. The SPEM measurements were performed using a spherical grating monochromator with four interchangeable gratings. The monochromator had a Fresnel zone plate (ZP) with an order-selection aperture, a flexure scanning stage and a hemispherical electron-analyzer system. A hemispherical analyzer with a 16-channel multichannel detector was used to collect photoelectrons. The valence-band SPEM spectra were calibrated using the E_F of a clean gold metal, and the energy of the incident X-rays was fixed at 380 eV with the energy resolution set to ~0.1 eV. Synchrotron-radiation-based XEOL spectra were obtained at the undulator-based spherical-grating monochromator beamline at the CLS, Saskatchewan, Canada. The XEOL spectra were collected using a dispersive spectrometer and were measured by collecting the total (zero order, 200–950 nm) and wavelength-selected luminescence as the excitation-photon energy was tuned across the O K-edge and Zn $L_{3,2}$-edge absorption. The O K-edge STXM and the corresponding XANES spectra were also obtained at the SM beamline of the CLS and at the 4U beamline of the UVSOR facility of the Institute for Molecular Science, Okazaki, Japan. In the STXM mapping measurements, the monochromatic X-ray beam was focused using a Fresnel ZP to a ~30 nm spot on the sample, and the sample was raster-scanned with synchronized detection of transmitted X-rays to generate a sequence of images (stacks) over the range of photon energies of interest; the transmitted beam intensities were measured at the image pixels. Energy scans were performed stepwise through the regions of interest with a typical resolving power ($E/\Delta E$) of ~1×10^4. The samples of ZnO NCs and NWs were gently scratched from the substrate and dispersed in ~1 ml of methanol to form ~1% suspensions, which were sonicated for ~1 min. Double-sided carbon tape was used to tape two blank Si_3N_4 windows onto the sample plate. Then, a tiny drop (<1 μl) of each of the ZnO NC and NW suspensions was placed onto each Si_3N_4 window. The samples were allowed to dry in air and then transferred into the STXM chamber for measurement. The O K-edge STXM-XANES image stacks were normalized to an empty area of the same stacks. The STXM data were analyzed using aXis2000 (available free for non-commercial applications at http://unicorn.mcmaster.ca/aXis2000.html) and PCA_GUI (available free at http://www.xray1.physics.sunysb.edu/data/software.php). The magnetization measurements of the ZnO NCs and NWs were performed using a superconducting quantum interference device magnetometer.

Results and discussion

Fig. 1(a) presents the Fourier-transformed (FT) $k^3\chi$ data from the Zn K-edge EXAFS of ZnO NC, NW and powder samples. The FT spectra include two main features at ~1.8 Å and 3.1 Å (without phase correction), which correspond to the nearest-neighbor (NN) Zn–O and Zn–Zn bond distances in ZnO nanostructures,[33] respectively. Clearly, the main features in the FT spectra at the Zn K-edges of the NCs and NWs are similar to those in the spectrum of the powder sample, indicating a similarity between the local atomic structures around the Zn sites in the ZnO nanostructures and the powder. The intensity of the first main feature (Zn–O bond distance) in the FT spectrum of the ZnO NCs is almost the same as that of the NWs, while the second main feature (Zn–Zn bond distance) is considerably lower than that of the NWs, as shown in Fig. 1(a). The qualitative analysis of the EXAFS data suggests that either a deficient coordination number of the Zn atoms or higher disordering of the atomic structure in the second shell around the Zn atoms in ZnO NCs with respect to the NW and powder samples. The reference (ZnO powder) sample shows a highly disordered structure compared to ZnO NCs and NWs, and the growth condition is possibly the reason for such a disordered structure of the ZnO powder. The lower inset in Fig. 1(a) presents the X-ray diffraction patterns of the ZnO NC, NW and powder samples. The enhancement of the (002) peak intensity and the drop in the (101) peak intensity of the ZnO NC and the NW relative to the powder sample reveal the preferred orientation of the *c* axis in the nanostructures. The shift in the (002) peak position of ZnO NCs and NWs compared to ZnO powder can be related to the substrate effect (lattice mismatch FTO/ZnO ~1.6% of ZnO NCs and NWs).[34] The upper insets in Fig. 1(a) display top-view and cross-sectional scanning electron microscopic (SEM) images of ZnO NCs and NWs. The images show that the diameters of the NCs and NWs in ZnO are approximately 130 nm and 100 nm, and their lengths are approximately 2.8 μm and 3.1 μm, respectively. Apparently, the spine-like structures developed from the etched pit on the ZnO NCs, which exhibits a more defective structure than the NWs, as observed from the FT spectra at the Zn K-edge. The details of the synthesis, morphology and characterization of the ZnO NCs and NWs can be found elsewhere.[32] The inset in Fig. 1(b) presents the *M–H* curves of the ZnO NCs and NWs, measured at 300 K (the diamagnetic character of the ZnO powder sample is not shown here). A magnetic field was applied parallel to the direction of growth of the sample, along the *c* axis (schematic inset I). The inset II in Fig. 1(b) magnifies the *M–H* curves for clarity. This inset demonstrates that the saturation magnetization (M_s) and coercivity (H_c) of ZnO NCs exceed those of the NWs. The values of M_s and H_c are approximately 3.0 emu cm^{-3} and 200 Oe, respectively, for ZnO NCs and 2.3 emu cm^{-3} and 100 Oe for NWs. The enhancement of the M_s of the ZnO NCs relative to that of the NWs can be attributed to the higher population of defects in ZnO NCs, as identified previously *via* PL measurements of capped ZnO NPs.[15] The low temperature CBD method used to fabricate ZnO NCs compared to NWs was attributed to the origin of the higher saturation magnetization and defect concentration in NCs. The EXAFS study also supports these arguments. The use of PL to determine the role of defects and vacancies in magnetism has been widely studied.[35–38] Fig. 1(b) presents the PL spectra of ZnO NCs and NWs, which exhibit two features – one with a sharp peak at ~380 nm and another broad feature that is centered at ~580 nm that are typically attributed to a near-band-edge transition and the emission that is caused by defects and vacancies, respectively. Although the involvement of defects such as V_O,[34] V_{Zn} (ref. 37) and oxygen antisites[39] in green (~520 nm) luminescence in

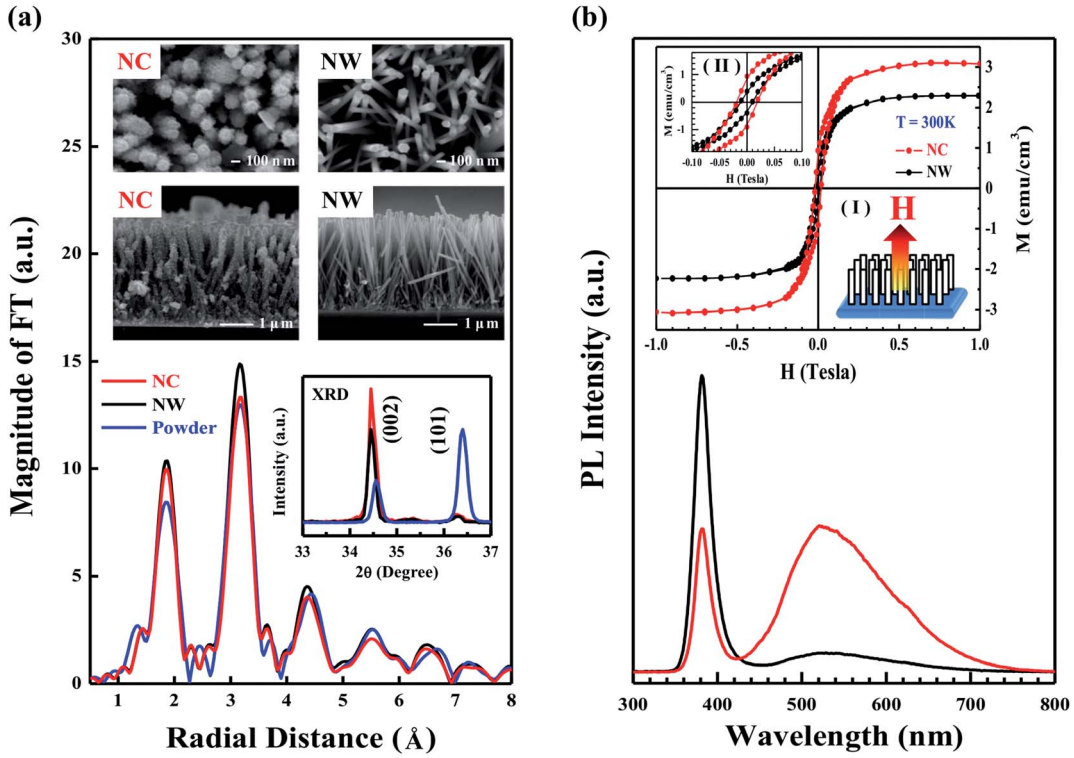

Fig. 1 (a) Fourier-transformed $k^3\chi$ data of Zn K-edge EXAFS measurements from $k = 3.0$ to 13.0 Å (not shown here). The insets show top-view and cross-sectional SEM images and the XRD patterns of ZnO NC, NW and powder samples. (b) PL spectra and M–H plots of ZnO NCs and NWs. Insets I and II present the magnetic field applied parallel to the growth direction (c axis) and the magnified M–H loops of ZnO NCs and NWs, respectively, at 300 K.

ZnO is still debated, Janotti *et al.*[37] have reported that based on DFT-LDA calculations, defects of the low formation energy of V_{Zn} are the primary sources of green luminescence in ZnO.

For more element-specific PL analysis, the synchrotron-radiation-based XEOL experiments were performed, in which optical emissions were followed by the X-ray excitation of core electrons in a process different from conventional PL.[39–41] XEOL is an element-specific probe and can determine direct correlations between the optical properties and electronic structures of nanomaterials.[42] Fig. 2(a) and (b) present the O K-edge XEOL spectra of ZnO NCs and NWs, respectively, under excitation energies in the range of 520–580 eV. The O K-edge XEOL spectrum of ZnO NCs has a sharp peak at ~380 nm and a strong broad feature that is centered at ~580 nm. The spectrum of ZnO NWs also exhibits a sharp peak at ~380 nm and a weak broad feature in the region of ~580 nm. As stated above, the sharp peak is attributed to a near-band-edge transition, while the broad feature is related to defects and/or vacancies in ZnO nanostructures. Fig. 2(c) and (d) present the Zn $L_{3,2}$-edge XEOL spectra of ZnO NCs and NWs, respectively, under excitation energies in the range of 1010–1050 eV. Similarly, the Zn $L_{3,2}$-edge XEOL spectrum of ZnO NCs has a sharp near-band-edge emission peak at ~380 nm and a strong broad feature that is centered at ~580 nm, whereas the corresponding spectrum of ZnO NWs exhibits a near-band-edge emission peak and a weak broad feature that is similar to that present in the O K-edge XEOL spectrum. Fig. 2(e) schematically shows the O K-edge and Zn $L_{3,2}$-edge XEOL processes of ZnO nanostructures, showing that when core electrons are excited by photons of a suitable energy ($E = h\nu$), the core electrons from both the O 1s and Zn 2p states are primarily excited to unoccupied O 2p and Zn 4 d/s states by O K-edge and Zn $L_{3,2}$-edge absorptions, respectively. The excited electrons in the conduction band further first relax non-radiatively or thermalize[41] (dotted arrows) and then undergo a near-band-edge transition, which corresponds to the sharp emission peak at ~380 nm in the O K-edge and Zn $L_{3,2}$-edge XEOL spectra [blue solid arrow, indicating the band gap (E_g) of ~3.3 eV in ZnO], similar to that observed in the conventional PL spectra as shown in Fig. 1(b). Meanwhile, the radiative emission related to defects and/or vacancies yields the strong (weak) broad-emission feature in the region of 520–670 nm in O K-edge and Zn $L_{3,2}$-edge XEOL spectra of ZnO NCs (NWs), which are indicated by the green/yellow arrows as shown in Fig. 2(e). Clearly, the O K-edge and Zn $L_{3,2}$-edge XEOL results reveal that the population of defects and/or vacancies in ZnO NCs is much higher than that in the NWs and is consistent with the results of conventional PL [Fig. 1(b)]. Importantly, the emission intensity of the broad feature that is associated with defects and/or vacancies in the O K-edge XEOL spectrum exceeds that of the sharp peak that is associated with the near-band-edge transition in ZnO NCs. However, such a difference in emission intensity is not observed in the Zn $L_{3,2}$-edge XEOL spectrum of ZnO NCs, in which the intensity of the broad feature is weaker than that of the sharp peak. Overall, the ratio

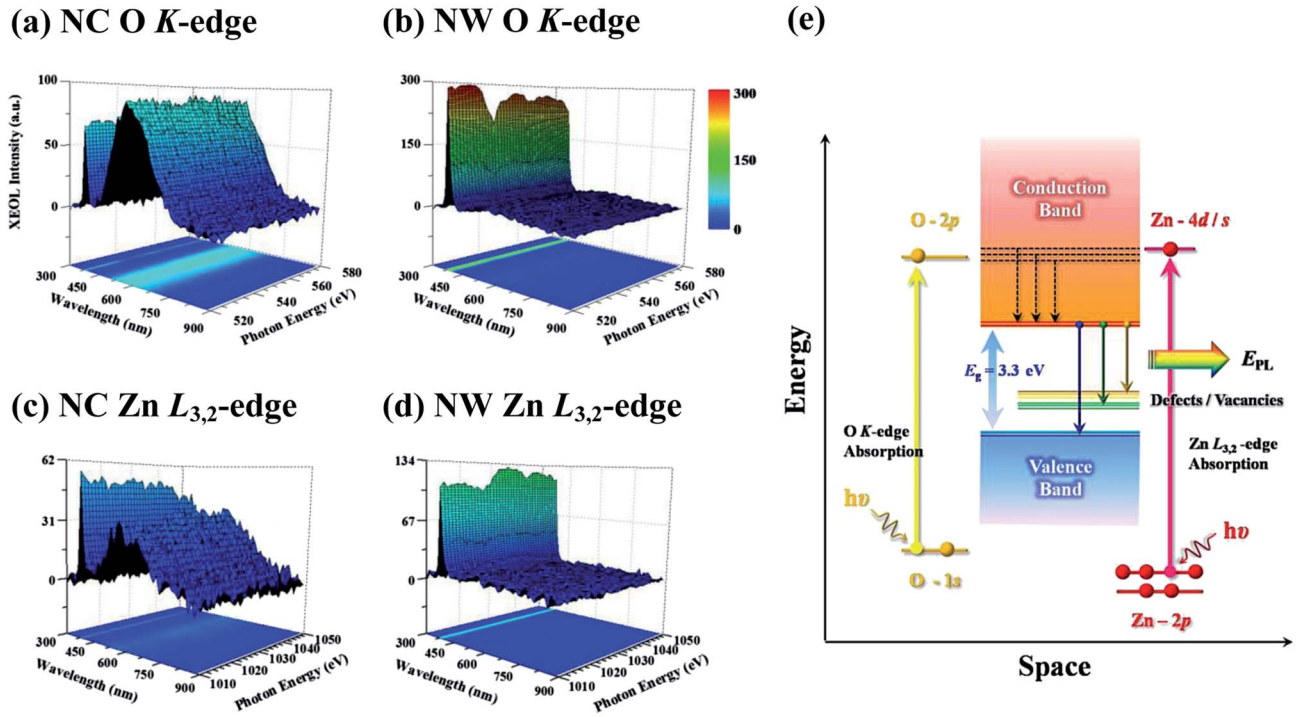

Fig. 2 (a and b) O K-edge XEOL spectra of ZnO NCs and NWs, respectively, under excitation at various energies in the range of 520–580 eV. (c and d) Zn $L_{3,2}$-edge XEOL spectra of ZnO NCs and NWs, respectively, under excitation at various energies in the range of 1010–1050 eV. (e) Schematic of the O K-edge and Zn $L_{3,2}$-edge XEOL processes in ZnO nanostructures.

of peak intensity of 580 : 380 nm is almost 1.5 : 1 and 1 : 2 in O K-edge and Zn $L_{3,2}$-edge of ZnO NCs, respectively. The results clearly suggest that the population of defects associated with V_{Zn} at the O sites in ZnO NCs is greater than that of the defects associated with V_O at the Zn sites. Combining the EXAFS, PL, O K-edge and Zn $L_{3,2}$-edge XEOL measurements reveals that ZnO NCs contain more defects than the NWs do, further suggesting that the number of defects of V_{Zn} at the O sites in ZnO NCs is larger than that of the defects of V_O at the Zn sites.

Fig. 3(a) and (b) display the O K-edge STXM stack mappings of randomly selected sample regions of ZnO NCs and NWs (upper left panel). The stack mappings are decomposed into blue, green and red maps (lower left panel), which correspond to the regions that are associated with different thicknesses and spectroscopic variations of the samples. Overall, the divisions of the mappings into thick (blue), thin (green) and impurity (red) regions were generated *via* principle component analysis (PCA) for cluster analysis based on spectroscopic differences. The PCA spectra for those three regions are the average spectra from all image pixels in each region. A more intense average spectrum generally means that the sample thickness is higher, where all types of chemical species in that region contribute to the thickness. The PCA cluster analysis indicated that the blue and green regions contain pure and predominantly pure ZnO (or more crystalline ZnO), respectively, and the red region represents the presence of significant impurities or surface/edge structures. However, the possibility that some thinner regions and impurities may be folded to form thick regions in ZnO nanostructures cannot be excluded. The background is shown in grey; the optical density or absorbance of the background is nearly zero, corresponding to the near-null intensity of the O K-edge and Zn $L_{3,2}$-edge STXM-XANES spectra. More details regarding STXM measurement and the analysis of data concerning various nanomaterials can be found elsewhere.[30,31,43] Clearly, the stack images of the O K-edge STXM maps that contain blue (thick), green (thin) and red (impurity) regions in ZnO NCs are distributed more randomly than those of the NWs because of their spine-like structures that are formed at the etched pits on the ZnO NCs, as seen from the SEM image [inset in Fig. 1(a)]. The O K-edge STXM-XANES spectra in the right-hand panels are the sum of the corresponding XANES spectra from the blue, green and red regions, which are presented in the lower left panels in Fig. 3(a) and (b). The general line shapes and positions of the features in the O K-edge STXM-XANES spectra are consistent with the features in the O K-edge XANES spectra of aligned ZnO nanorods (NR) obtained in the author's previous studies.[44,45] According to the dipole-transition selection rule, the features at ~535 to 550 eV, which are denoted by A_1–D_1 in the O K-edge STXM-XANES spectra, are attributed to the electron excitations from O 1s-derived states to $2p_\sigma$-derived (along the bilayer) and O $2p_\pi$-derived (along the *c* axis) states, which are approximately proportional to the density of the unoccupied O 2p-derived states. The enhancements of the features A_1–D_1 represent the enhanced local densities of states (DOSs) that arise from the defects or dangling bonds in the tip region in aligned ZnO NRs.[44] A similarly enhanced local DOS in the tip region has also been observed in aligned carbon nanotubes (CNTs).[46] However, as displayed in the right-hand panel in

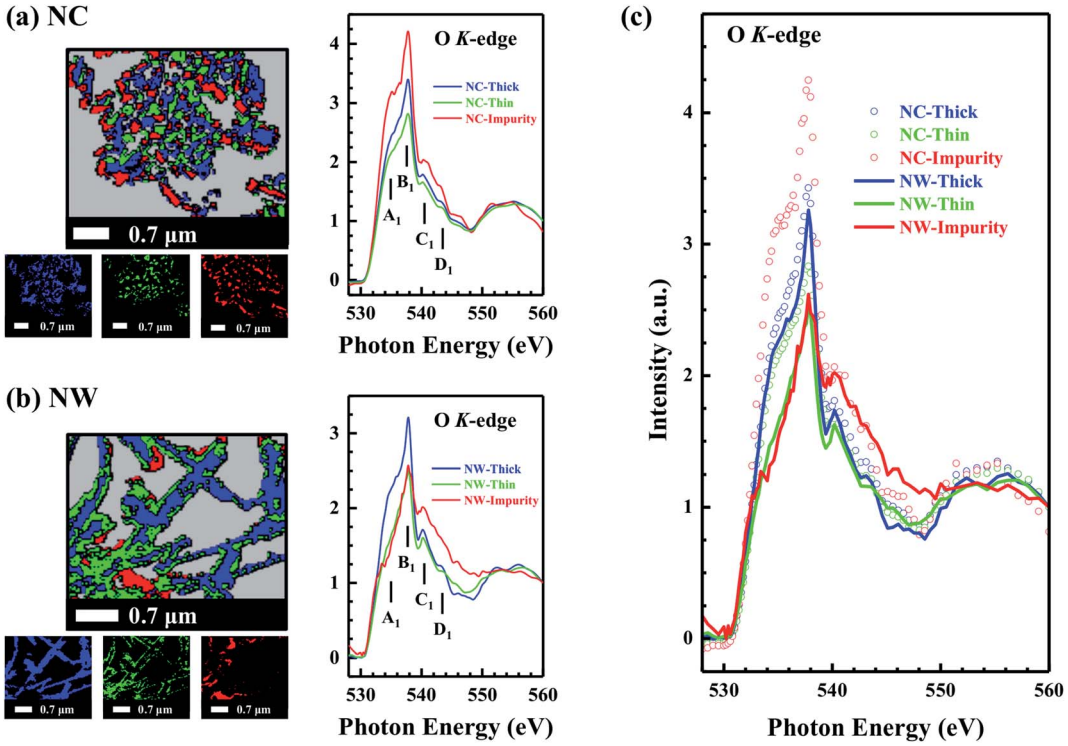

Fig. 3 (a and b) O K-edge STXM and the corresponding XANES spectra of ZnO NCs and NWs, respectively. The top left panels in (a) and (b) present stacked images of the target region with different thickness indices (blue, green and red), which correspond to the maps of the thick, thin and impurity/edge regions in the left-hand sides of the lower panels, respectively. The right-hand sides of (a) and (b) present the sums of the XANES spectra of the differently colored (blue, green and red) regions. (c) Comparison of the O K-edge STXM-XANES spectra of the thick, thin and impurity/edge regions of ZnO NCs with those of the NWs.

Fig. 3(a), the O K-edge STXM-XANES spectra clearly reveal that the intensities of features A_1–D_1 in the impurity region of ZnO NCs are higher than those in the other two regions. The enhanced intensities of the features A_1–D_1 in the O K-edge STXM-XANES spectra can result in a higher population of defects in the impurity or surface/edge region because of the non-stoichiometric (relative concentration of Zn : O ≠ 1 : 1) chemical composition or dangling bonds. Accordingly, the local DOS at the O sites in ZnO NCs is enhanced, in a manner similar to the enhancement of the local DOS in the tip region in aligned ZnO NRs and CNTs.[44,46] Surprisingly, for ZnO NWs, the intensities of features C_1 and D_1 and the intensities of features A_1 and B_1 were found to be higher and lower, respectively, in the impurity region than in the thick region, as illustrated in the right-hand panel in Fig. 3(b). This phenomenon may arise from the fact that the O K-edge STXM-XANES spectra of ZnO NWs are highly sensitive to the orientation of the wurtzite structure of the ZnO with respect to the angle of incidence of the photon or electric polarization[44] or from the fact that the impurity region in NWs are chemically different from that in NCs. To compare the intensities of the STXM-XANES features in the regions of different thicknesses in ZnO NCs with the intensities of those in the NWs, Fig. 3(c) shows the O K-edge STXM-XANES spectra in the thick, thin and impurity regions of ZnO NCs and NWs. Apparently, the feature intensity in the impurity region of ZnO NCs is much higher than in the NWs, indicating that more defects and/or vacancies (or dangling bonds) are present at O sites in ZnO NCs than in the NWs. It also reveals the enhanced local DOS of O 2p at/above the conduction-band minimum (E_{CBM}) or the Fermi level (E_F) in ZnO NCs. This finding is consistent with the PL and O K-edge XEOL measurements described above. Notably, the intensities and line shapes of the features of the O K-edge STXM-XANES spectra in the thick region in ZnO NCs and NWs are almost the same, exhibiting an ideal wurtzite structure (no clear defects or dangling bonds at the O sites) in the thick region in both ZnO NCs and NWs.

The STXM-XANES spectra that are presented in Fig. 3(a) and (b) were obtained at the Canadian Light Source (CLS) in Saskatchewan, Canada, and confirm that the enhanced local DOSs or intensities of features in the O K-edge STXM-XANES spectra increased because of the higher population of defects and/or vacancies at the O sites in ZnO NCs than in the NWs. The O K-edge STXM spectra and the corresponding XANES spectra of the ZnO nanostructures were also obtained at the 4U beamline of the Ultraviolet Synchrotron Orbital Radiation (UVSOR) facility in Okazaki, Japan, verifying that the number of defects and/or vacancies at the O sites in ZnO NCs exceeds that in the NWs and further supporting the claim that the population of defects and/or vacancies at the O sites in ZnO nanostructures is closely related to the d^0 magnetism. Fig. 4(a)–(d) show the O K-edge STXM stack mappings for two randomly selected regions in ZnO NCs (NC-1 and NC-2) and NWs (NW-1 and NW-2), respectively,

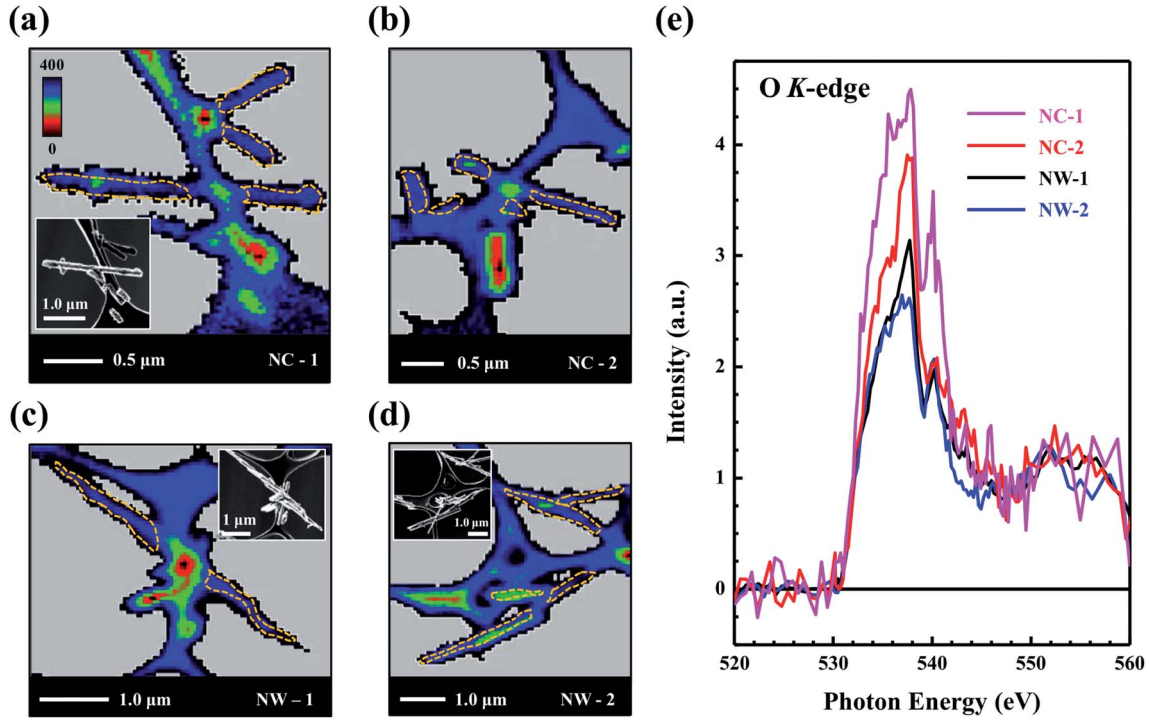

Fig. 4 (a)–(d) O K-edge STXM images of two selected regions in ZnO NCs (NC-1 and NC-2) and NWs (NW-1 and NW-2), respectively. (e) O K-edge STXM-XANES spectra of regions bordered by yellow dashed lines in ZnO NCs and NWs. The insets show the corresponding SEM images.

obtained from UVSOR. The insets in the figures also present the corresponding SEM images that help to identify the regions and can be used to verify the STXM images. To verify the signal-to-noise ratio of the XANES spectra obtained from specific mapping areas in the STXM images, the O K-edge STXM-XANES spectra in Fig. 4(e) were obtained as the sum of the XANES spectra in the regions that are bordered by yellow dashed lines, as shown in NC-1, NC-2, NW-1 and NW-2. The intensities of the O K-edge STXM-XANES spectra of NC-1 and NC-2 are clearly higher than those of NW-1 and NW-2; this result is similar to that of the STXM-XANES spectra in Fig. 3(c), which were obtained from the CLS; which consistently demonstrate that the population of defects and/or vacancies at the O sites in ZnO NCs is larger than in the NWs and confirming the enhanced DOS of O 2p-derived states, as the population of defects and/or vacancies (or dangling bonds) at/above E_{CBM} or E_F in ZnO NCs exceeds that in the NWs.

The defects or dangling bonds that are produced by topological defects close to the ends of aligned ZnO NRs, CNTs and graphene nanocones have been previously suggested to be responsible for the increase in the local DOSs at the tips or cone apices,[44–49] indicating that defects in bent vertical graphite sheets can yield localized states in the gap that are oriented in the direction of the field. The density of the O 2p-derived states are clearly enhanced in the impurity (or surface/edge) region at/above E_{CBM} or E_F, as was observed in ZnO NCs above. A similar enhancement of the DOS at/below the valence-band maximum (E_{VBM}) or E_F in ZnO NCs relative to that in the NWs was also be observed. Fig. S1 in the ESI† presents the valence-band DOSs at/below the E_{VBM} or E_F of ZnO NCs and NWs, which were obtained using spatially resolved SPEM.[50] Because the occupied states at/below E_{VBM} or E_F in ZnO nanostructures are dominated by defects (or dangling bonds) and/or anion-derived p states, which are O 2p-derived states, the strong enhancement of the feature near/below E_{VBM} or E_F in ZnO NCs is attributed to the higher DOS of the O 2p-derived states. Together, the results of O K-edge STXM-XANES spectroscopy (which was used to probe the local DOS at/above E_{CBM} or E_F) and the valence-band SPEM measurements (which were used to probe the local DOS at/below E_{VBM} or E_F) strongly support the claim that the superior d^0 magnetism in ZnO NCs with respect to that in the NWs is closely related to the enhancement of the DOS of O 2p-derived states close to E_F, because the population of defects and/or vacancies at the O sites in the impurity region in ZnO NCs is higher.

As direct evidence that the enhancement of the density of O 2p-derived states near E_F induces magnetization in ZnO nanostructures, Fig. 5(a) and (b) present the O K-edge and Zn $L_{3,2}$-edge XANES spectra of the ZnO NCs and NWs that were obtained in surface-sensitive electron-yield mode with the photon helicity of the incident X-rays parallel (μ^+) and anti-parallel (μ^-) to the direction of magnetization, respectively. The difference in μ^+ and μ^- intensities can be observed in the magnified O K-edge XANES spectra of ZnO NCs and NWs, which are presented in the lower and middle insets, respectively. The upper inset in Fig. 5(a) displays the O K-edge XMCD spectrum, $(\mu^+ - \mu^-)/(\mu^+ + \mu^-)$. The weak but confirmed magnetic moment at the O sites in ZnO NCs and NWs results in the imperfect

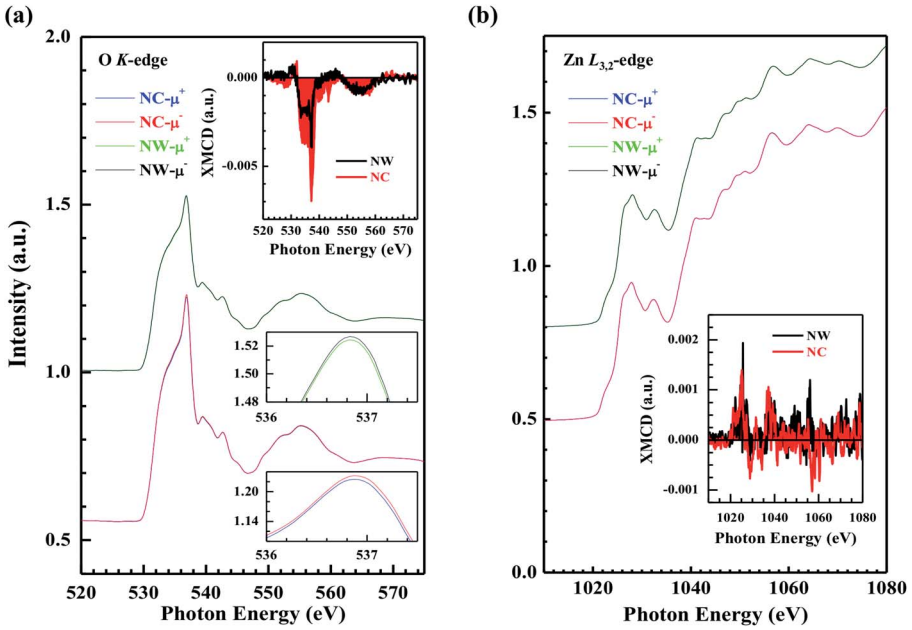

Fig. 5 (a) Normalized O K-edge and (b) Zn $L_{3,2}$-edge XANES spectra with the photon helicity of the incident X-rays parallel (μ^+) and anti-parallel (μ^-) to the direction of magnetization for ZnO NCs and ZnO NWs. The insets display the magnified O K-edge XANES spectra and the magnified O K-edge and Zn $L_{3,2}$-edge XMCD spectra of ZnO NCs and ZnO NWs, respectively.

alignment of the spin moments of O 2p electrons and/or dangling p bonds in the impurity region (each XMCD spectrum typically has been merged at least 20 scans together). The intensity of the O K-edge XMCD spectrum of ZnO NCs clearly exceeds that of the NWs. The maximum value of XMCD is approximately 7% in ZnO NCs and 4% in the NWs. This result is associated with the higher intensities of features A_1–D_1 in the O K-edge STXM-XANES spectrum and feature I in the valence-band SPEM spectra that are presented in Fig. 3(c), 4(e) and S1 (in the ESI†), evidently revealing that the larger magnetic moment at the O sites in ZnO NCs exceeds that in the NWs. This finding is also consistent with the *M*–*H* curves that are shown in the inset of Fig. 1(b). However, the Zn $L_{3,2}$-edge XANES spectra in Fig. 5(b) probe the unoccupied Zn s- and d-derived states, according to the dipole-transition selection rule. The Zn 3d orbital is fully occupied, so that the lowest unoccupied orbital of the Zn ion is Zn 4s, followed by Zn 4p and 4d. Accordingly, the features in the Zn $L_{3,2}$-edge XANES spectra are primarily associated with the transition of Zn 2p electrons to Zn 4 d/s-derived states.[44,45] In contrast, Fig. 5(b) reveals no clear magnetic moment of the Zn 4d states in either ZnO NCs or NWs and excludes the possibility of Zn d orbitals' role in d^0 magnetism in ZnO nanostructures. Therefore, combining the results of O K-edge and Zn $L_{3,2}$-edge XEOL, XMCD, O K-edge STXM-XANES and valence-band SPEM spectra reveals not only that the origin of d^0 magnetism in ZnO nanostructures is closely related to O 2p-derived states rather than Zn d orbitals but also that the higher magnetic moment is associated with the higher population of defects and/or vacancies in the impurity region in ZnO NCs compared with that in the NWs.

To verify the importance of enhanced O 2p states in the d^0 magnetism of ZnO nanostructures, we performed first-principles LDA + *U* calculations of defect- and/or vacancy-induced spontaneous spin polarization in bulk ZnO. A vacancy concentration of 2.8% was simulated by introducing an isolated neutral cation vacancy V_{Zn} and anion vacancy V_O (Fig. S2 in the ESI†), respectively, into a defect-free 72-atom wurtzite ZnO supercell ($Zn_{36}O_{36}$). Details of the computations can be found in the ESI.† To elucidate the origin of the defect- and/or vacancy-induced d^0 magnetization, the total and partial DOSs (TDOS and PDOS) of the native V_{Zn} in ZnO were calculated. The spin-polarized TDOS of V_{Zn} in ZnO ($Zn_{35}O_{36}$) was compared to that in defect-free bulk ZnO, as presented in the top panel of Fig. 6(a). The results of the calculations indicate that the majority spin (↑) defect states are fully occupied, whereas the minority states (↓) are partially occupied. Clearly, a net spin moment associated with the difference between the majority and minority spin densities is present in ZnO with V_{Zn}. A nearly negligible contribution of the asymmetric majority–minority spin density was derived from Zn 3d (t_{2g} and e_g); see the calculated PDOS of occupied Zn 3d orbitals in the middle panel of Fig. 6(a). Indeed, careful analysis of the calculated PDOS indicated that the dangling or unpaired O 2p orbitals of the four NN tetrahedral O sites (O_{2p}^{NN}) around each defect/vacancy center are responsible for most (>75%) of the V_{Zn}-induced local magnetic moment (1.65 μ_B), as shown in the yellow areas of the bottom panel in Fig. 6(a). To visualize the effects of a defect on both electronic and local structures, the spin-density distribution of a 72-atom ZnO with one defect (V_{Zn}) is presented in Fig. 6(b), in which the net spin density is represented as yellow isosurfaces near the defect and/or vacancy center, and the Zn and O atoms are shown as blue and red spheres, respectively. The removal of a Zn atom (V_{Zn}) from the ZnO results in four dangling or unpaired O bonds. These dangling or unpaired bonds cause a significant

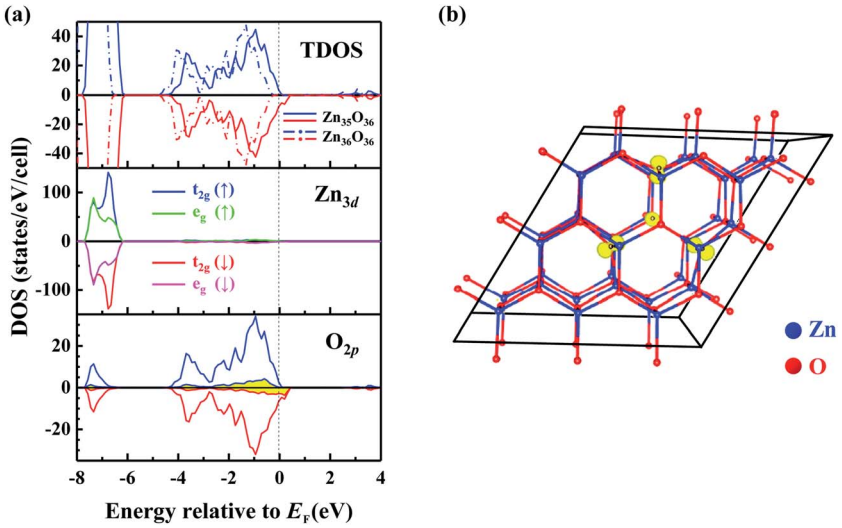

Fig. 6 (a) Calculated TDOS (top panel) and PDOSs of Zn 3d (middle panel) and O 2p (bottom panel) of wurtzite ZnO with V_{Zn} ($Zn_{35}O_{36}$). The TDOS of defect-free bulk ZnO ($Zn_{36}O_{36}$, indicated by dotted lines) is also shown in the top panel for comparison. (b) Calculated Jahn–Teller distortion of the native defect V_{Zn} in a 72-atom supercell of wurtzite ZnO. The net spin density (defined as the difference between the majority spin density and the minority spin density) is indicated by yellow isosurfaces near the defect center. Zn and O atoms are depicted as blue and red spheres, respectively. E_F, denoted by the dashed line, is aligned to 0 eV.

Jahn–Teller distortion (displacing four NN O atoms outward from their original wurtzite symmetrical sites and away from the defect and/or vacancy center), reducing the local magnetic moment from the ideal value of 2 μ_B to 1.65 μ_B. Our calculated result suggests a slightly larger value of the magnetic moment than Wang *et al.* predicted for V_{Zn} on the surface of ZnO thin films (1.5 μ_B),[25] the additional NN coordination of O atoms around the defect center in a bulk system in comparison with a surface configuration possibly the reason. Additionally, the formation of a V_{Zn}-induced local magnetic moment can be predicted *via* Stoner's band theory,[51,52] in which itinerant ferromagnetism can be stabilized when the gain in exchange energy is greater than the loss in kinetic energy of itinerant electrons. According to the results based on calculations of the Stoner parameter and TDOS at/near E_F (Fig. S3 in the ESI†), stable spontaneous ferromagnetism due to V_{Zn} in ZnO can be obtained. This calculation is consistent with the results of the O K-edge XMCD and STXM-XANES presented above and the valence-band SPEM presented in the ESI.† Indeed, such profound cation-vacancy-induced magnetism, associated mainly with the spatial local character of the 2p states of the NN anion sites around the defect and/or vacancy centers, has also been found in other first-row d^0 semiconductors.[53,54] However, the anion vacancy, V_O, does not contribute significantly to the local spin moment. The symmetry of the different spin states is preserved for V_O in ZnO (Fig. S2 in the ESI;† the TDOS and PDOS plots of the native V_O in ZnO are shown in detail). Accordingly, the origin of d^0 magnetization in ZnO nanostructures is related to the presence of dangling/unpaired O 2p states. Nonetheless, the existence of defects and/or vacancies does not suffice to induce macroscopic magnetization. Stated otherwise, intrinsic defects and/or vacancies may cause spin polarization but not necessarily macroscopic magnetization. For example, the defects and/or vacancies at Zn sites in ZnO NCs that were also observed in the Zn $L_{3,2}$-edge XEOL spectra, which do not exhibit macroscopic magnetization behavior or a spin moment, originate from Zn d orbitals, as demonstrated by the null Zn $L_{3,2}$-edge XMCD that is presented in the inset in Fig. 5(b). This difference in magnetism may arise from the fact that the population of defects and/or vacancies may not be sufficient to allow both a ferromagnetic interaction and a lack of preservation of long-range coupling between dangling or unpaired bonds at Zn sites in ZnO.[28,29] Again, the above conclusions are based on calculations for a bulk ZnO system. For low-dimensional systems, such as ZnO NCs and NWs, the possibility that more complicated orbital hybridizations may contribute to non-negligible magnetic properties cannot be excluded.

Conclusion

In summary, the presence of more defects/vacancies in ZnO NCs than in the NWs was observed and confirmed *via* EXAFS, PL and XEOL measurements. The low temperature CBD method used to fabricate NCs compared to NWs was attributed to the origin of the higher saturation magnetization and defect concentration in NCs. Specifically, O K-edge STXM mappings reveal that in ZnO NCs, the defects and/or vacancies were located primarily in the impurity or surface/edge (non-stoichiometric) region rather than in the thick (core) region; the local DOS at/near E_F, as determined from the O K-edge STXM-XANES and valence-band SPEM spectra of ZnO NCs, was enhanced. The increased density of O 2p-derived states in ZnO NCs plays an important role in inducing d^0 magnetism. The experimental XMCD results presented herein also demonstrate that the magnetic moments arise from the O 2p orbitals in ZnO nanostructures rather than from Zn d orbitals. Theoretically,

LDA + U calculations further support the conclusion that the presence of defects and/or vacancies or dangling/unpaired 2p bonds at O sites around cation vacancy (V_{Zn}) centers is responsible for d^0 magnetism in ZnO.

Acknowledgements

The authors H. C. H., J. W. C. and W. F. P. acknowledge the National Science Council of Taiwan for financial support under Contract No. NSC 102-2112-M-032-001. HCH also thanks NCTS of Taiwan for support. The Canadian Light Source was supported by the Natural Sciences and Engineering Research Council of Canada, the National Research Council Canada, the Canadian Institutes of Health Research, the Province of Saskatchewan, Western Economic Diversification Canada, and the University of Saskatchewan.

References

1 T. Dietl, *Nat. Mater.*, 2010, **9**, 965–974.
2 J. M. D. Coey, M. Venkatesan and C. B. Fitzgerald, *Nat. Mater.*, 2005, **4**, 173–179.
3 S. Kuroda, N. Nishizawa, K. Takita, M. Mitome, Y. Bando, K. Osuch and T. Dietl, *Nat. Mater.*, 2007, **6**, 440–446.
4 J. Philip, A. Punnoose, B. I. Kim, K. M. Reddy, S. Layne, J. O. Holmes, B. Satpati, P. R. Leclair, T. S. Santos and J. S. Moodera, *Nat. Mater.*, 2006, **5**, 298–304.
5 S. Chambers, *Nat. Mater.*, 2010, **9**, 956–957.
6 M. Venkatesan, C. B. Fitzgerald and J. M. D. Coey, *Nature*, 2004, **430**, 630.
7 S. Z. Deng, H. M. Fan, M. Wang, M. R. Zheng, J. B. Yi, R. Q. Wu, H. R. Tan, C. H. Sow, J. Ding, Y. P. Feng, *et al.*, *ACS Nano*, 2010, **4**, 495–505.
8 J. I. Hong, J. Choi, S. S. Jang, J. Gu, Y. Chang, G. Wortman, R. L. Snyder and Z. L. Wang, *Nano Lett.*, 2012, **12**, 576–581.
9 L. Kou, C. Li, Z. Zhang and W. Guo, *ACS Nano*, 2010, **4**, 2124–2128.
10 A. Sundaresan, R. Bhargavi, N. Rangarajan, U. Siddesh and C. N. R. Rao, *Phys. Rev. B: Condens. Matter Mater. Phys.*, 2006, **74**, 161306.
11 S. B. Singh, M. V. Limaye, S. K. Date, S. Gokhale and S. K. Kulkarni, *Phys. Rev. B: Condens. Matter Mater. Phys.*, 2009, **80**, 235421.
12 M. S. Seehra, P. Dutta, S. Neeleshwar, Y. Y. Chen, C. L. Chen, S. W. Chou, C. C. Chen, C. L. Dong and C. L. Chang, *Adv. Mater.*, 2008, **20**, 1656–1660.
13 Y. Yamamoto, T. Miura, M. Suzuki, N. Kawamura, H. Miyagawa, T. Nakamura, K. Kobayashi, T. Teranishi and H. Hori, *Phys. Rev. Lett.*, 2004, **93**, 116801.
14 J. Bartolomé, F. Bartolomé, L. García, A. Figueroa, A. Repollés, M. Martínez-Pérez, F. Luis, C. Magén, S. Selenska-Pobell, F. Pobell, *et al.*, *Phys. Rev. Lett.*, 2012, **109**, 247203.
15 M. A. Garcia, J. M. Merino, E. Fernández Pinel, A. Quesada, J. de la Venta, M. L. Ruíz González, G. R. Castro, P. Crespo, J. Llopis, J. M. González-Calbet, *et al.*, *Nano Lett.*, 2007, **7**, 1489–1494.
16 M. Gacic, G. Jakob, C. Herbort, H. Adrian, T. Tietze, S. Brück and E. Goering, *Phys. Rev. B: Condens. Matter Mater. Phys.*, 2007, **75**, 205206.
17 X. Xu, C. Xu, J. Dai, J. Hu, F. Li and S. Zhang, *J. Phys. Chem. C*, 2012, **116**, 8813–8818.
18 K. R. Kittelstved, W. K. Liu and D. R. Gamelin, *Nat. Mater.*, 2006, **5**, 291–297.
19 G. Z. Xing, Y. H. Lu, Y. F. Tian, J. B. Yi, C. C. Lim, Y. F. Li, G. P. Li, D. D. Wang, B. Yao, J. Ding, *et al.*, *AIP Adv.*, 2011, **1**, 022152.
20 M. Khalid, M. Ziese, A. Setzer, P. Esquinazi, M. Lorenz, H. Hochmuth, M. Grundmann, D. Spemann, T. Butz, G. Brauer, *et al.*, *Phys. Rev. B: Condens. Matter Mater. Phys.*, 2009, **80**, 035331.
21 D. J. Keavney, D. B. Buchholz, O. Ma and R. P. H. Chang, *Appl. Phys. Lett.*, 2007, **91**, 012501.
22 J. Chaboy, R. Boada, C. Piquer, M. Laguna-Marco, M. García-Hernández, N. Carmona, J. Llopis, M. Ruíz-González, J. González-Calbet, J. Fernández, *et al.*, *Phys. Rev. B: Condens. Matter Mater. Phys.*, 2010, **82**, 064411.
23 C. Guglieri, M. A. Laguna-Marco, M. A. García, N. Carmona, E. Céspedes, M. García-Hernández, A. Espinosa and J. Chaboy, *J. Phys. Chem. C*, 2012, **116**, 6608–6614.
24 Q. Wang, Q. Sun, G. Chen, Y. Kawazoe and P. Jena, *Phys. Rev. B: Condens. Matter Mater. Phys.*, 2008, **77**, 205411.
25 G. Fischer, N. Sanchez, W. Adeagbo, M. Lüders, Z. Szotek, W. M. Temmerman, A. Ernst, W. Hergert and M. C. Muñoz, *Phys. Rev. B: Condens. Matter Mater. Phys.*, 2011, **84**, 205306.
26 A. N. Morozovska, E. A. Eliseev, M. D. Glinchuk and R. Blinc, *Phys. B*, 2011, **406**, 1673–1688.
27 I. S. Elfimov, S. Yunoki and G. A. Sawatzky, *Phys. Rev. Lett.*, 2002, **89**, 216403.
28 C. Peng, Y. Liang, K. Wang, Y. Zhang, G. Zhao and Y. Wang, *J. Phys. Chem. C*, 2012, **116**, 9709–9715.
29 R. Podila, W. Queen, A. Nath, J. T. Arantes, A. L. Schoenhalz, A. Fazzio, G. M. Dalpian, J. He, S. J. Hwu, M. J. Skove, *et al.*, *Nano Lett.*, 2010, **10**, 1383–1386.
30 J. G. Zhou, J. Wang, C. L. Sun, J. M. Maley, R. Sammynaiken, T. K. Sham and W. F. Pong, *J. Mater. Chem.*, 2011, **21**, 14622–14630.
31 J. Wang, J. Zhou, Y. Hu and T. Regier, *Energy Environ. Sci.*, 2013, **6**, 926–934.
32 C. T. Wu and J. J. Wu, *J. Mater. Chem.*, 2011, **21**, 13605–13610.
33 S. C. Ray, Y. Low, H. M. Tsai, C. W. Pao, J. W. Chiou, S. C. Yang, F. Z. Chien, W. F. Pong, M. H. Tsai, K. F. Lin, *et al.*, *Appl. Phys. Lett.*, 2007, **91**, 263201.
34 Y. Xia, Y. Zhang, X. Yu and F. Chen, *CrystEngComm*, 2014, **16**, 5394–5401.
35 G. Xing, D. Wang, J. Yi, L. Yang, M. Gao, M. He, J. Yang, J. Ding, T. C. Sum and T. Wu, *Appl. Phys. Lett.*, 2010, **96**, 112511.
36 D. Wang, Q. Chen, G. Xing, J. Yi, S. R. Bakaul, J. Ding and T. Wu, *Nano Lett.*, 2012, **12**, 3994–4000.
37 A. Janotti and C. G. V. Walle, *Phys. Rev. B: Condens. Matter Mater. Phys.*, 2007, **76**, 165202.
38 B. Lin, Z. Fu and Y. Jia, *Appl. Phys. Lett.*, 2001, **79**, 943–945.

39 T. K. Sham and R. A. Rosenberg, *ChemPhysChem*, 2007, **8**, 2557–2567.
40 L. Liu, T. K. Sham, W. Han, C. Zhi and Y. Bando, *ACS Nano*, 2011, **5**, 631–639.
41 L. Armelao, F. Heigl, S. Brunet, R. Sammynaiken, T. Regier, R. I. R. Blyth, L. Zuin, R. Sankari, J. Vogt and T. K. Sham, *ChemPhysChem*, 2010, **11**, 3625–3631.
42 J. W. Chiou, S. C. Ray, S. I. Peng, C. H. Chuang, B. Y. Wang, H. M. Tsai, C. W. Pao, H. J. Lin, Y. C. Shao, Y. F. Wang, *et al.*, *J. Phys. Chem. C*, 2012, **116**, 16251–16258.
43 C. L. Sun, C. T. Chang, H. H. Lee, J. Zhou, J. Wang, T. K. Sham and W. F. Pong, *ACS Nano*, 2011, **5**, 7788–7795.
44 J. W. Chiou, J. C. Jan, H. M. Tsai, C. W. Bao, W. F. Pong, M. H. Tsai, I. H. Hong, R. Klauser, J. F. Lee, J. J. Wu, *et al.*, *Appl. Phys. Lett.*, 2004, **84**, 3462–3464.
45 J. W. Chiou, K. P. K. Kumar, J. C. Jan, H. M. Tsai, C. W. Bao, W. F. Pong, F. Z. Chien, M. H. Tsai, I. H. Hong, R. Klauser, *et al.*, *Appl. Phys. Lett.*, 2004, **85**, 3220–3222.
46 J. W. Chiou, C. L. Yueh, J. C. Jan, H. M. Tsai, W. F. Pong, I. H. Hong, R. Klauser, M. H. Tsai, Y. K. Chang, Y. Y. Chen, *et al.*, *Appl. Phys. Lett.*, 2002, **81**, 4189–4191.
47 D. L. Carroll, P. Redlich, P. M. Ajayan, J. C. Charlier, X. Blase, A. D. Vita and R. Car, *Phys. Rev. Lett.*, 1997, **78**, 2811–2814.
48 P. Kim, T. W. Odom, J. L. Huang and C. M. Lieber, *Phys. Rev. Lett.*, 1999, **82**, 1225–1228.
49 F. S. Hage, Q. M. Ramasse, D. M. Kepaptsoglou, Ø. Prytz, A. E. Gunnaes, G. Helgesen and R. Brydson, *Phys. Rev. B: Condens. Matter Mater. Phys.*, 2013, **88**, 155408.
50 S. C. Ray, J. W. Chiou, W. F. Pong and M. H. Tsai, *Crit. Rev. Solid State Mater. Sci.*, 2006, **31**, 91–110.
51 E. C. Stoner, *Proc. R. Soc. London, Ser. A*, 1938, **165**, 372–414.
52 E. C. Stoner, *Proc. R. Soc. London, Ser. A*, 1938, **169**, 339–371.
53 X. Peng, H. J. Xiang, S. H. Wei, S. S. Li, J. B. Xia and J. Li, *Phys. Rev. Lett.*, 2009, **102**, 017201.
54 P. Dev, Y. Xue and P. Zhang, *Phys. Rev. Lett.*, 2008, **100**, 117204.